



## Current–voltage characteristics of manganite based p–n interfaces: Role of swift heavy ion irradiation and defect annihilation

Alpa Zankat<sup>a</sup>, Keval Gadani<sup>b</sup>, Bhargav Rajyaguru<sup>a</sup>, Khushal Sagapariya<sup>a</sup>, Vivek Pachchigar<sup>c</sup>, M. Ranjan<sup>c</sup>, K. Asokan<sup>d</sup>, P.S. Solanki<sup>a</sup>, N.A. Shah<sup>a</sup>, D.D. Pandya<sup>e,\*</sup>

<sup>a</sup> Department of Physics, Saurashtra University, Rajkot, 360005, India

<sup>b</sup> Department of Physics, Center of Education, Indian Institute of Teacher Education, Gandhinagar, 382016, India

<sup>c</sup> FCIPT, Institute for Plasma Research, Bhat, Gandhinagar, 382428, Gujarat, India

<sup>d</sup> Inter University Accelerator Centre, Aruna Asaf Ali Marg, New Delhi, 110067, India

<sup>e</sup> Human Resource Development Centre, Saurashtra University, Rajkot, 360005, India

### ARTICLE INFO

#### Keywords:

Defects  
Current–voltage characteristics  
Surface morphology  
Irradiation  
Annihilation effect

### ABSTRACT

We report current–voltage (I–V) device characteristics of pulsed laser deposition (PLD) grown  $\text{La}_{0.5}\text{Gd}_{0.2}\text{Ca}_{0.3}\text{MnO}_3$  (LGCMO) manganite thin films on single crystalline (100)  $\text{Nb}:\text{SrTiO}_3$  (SNTO) substrates. LGCMO films were irradiated using 100 MeV  $\text{O}^{+9}$  swift heavy ions (SHI). The 0–20 X-ray diffraction (XRD) and atomic force microscopy (AFM) measurement were performed at room temperature, respectively, for understanding the structural and microstructural behaviors of the films. The current–voltage (I–V) data were taken under the bias voltage applied across LGCMO/SNTO p–n interfaces at room temperature. Observed I–V behaviors for all interfaces have been discussed in the context of lattice strain, grain size and grain boundary density. To study the effect of annihilation on the irradiated LGCMO films, 50 nm thick  $\text{ZnO}$  layer was grown on the surface of LGCMO/SNTO films using chemical solution deposition (CSD) method under oxygen environment with a controlled flow. XRD, AFM and I–V measurements were performed again for annealed  $\text{ZnO}/\text{LGCMO}$  interfaces. Observed I–V characteristics across  $\text{ZnO}/\text{LGCMO}$  interface have been discussed in details in the context of annihilation induced modifications in the interface, structural strain and surface morphology.

### 1. Introduction

Researchers and scientists are engaged with the development processes in almost all materials aspects for the betterment of society [1–14].  $\text{RMnO}_3$  (RMO) manganites, having  $\text{ABO}_3$  type perovskite structure, have been studied because of various interesting physical phenomena. By substituting divalent ions ( $\text{Ca}^{+2}$ ,  $\text{Sr}^{+2}$ ,  $\text{Ba}^{+2}$ , etc) as well as rare–earth ions ( $\text{Gd}^{+3}$ ,  $\text{Dy}^{+3}$ ,  $\text{Nd}^{+3}$ , etc) at A–site in RMO introduces structural disorder, electronic phase alterations and magnetic phase changes. All the above modifications have been understood for mixed valent manganites by using various fundamental aspects such as Jahn–Teller (J–T) distortion [15], crystal field theory (CFT) [16] and zener double exchange (ZDE) mechanism [17]. Mixed valent manganites exhibit insulator–metal (I–M) transition at  $T_p$  [18], paramagnetic–ferromagnetic (PM–FM) transition at  $T_c$  [19] and magnetoresistance (MR) behavior [20] that strongly depend upon stoichiometry [21–24] and substituted ion at A–site [25,26]. They have

been extensively studied in the form of single–crystalline thin film [27], polycrystalline thin film [28], nanostructured [29], composite [30], nanocomposite [31], polycrystalline bulk [32,33], device [34], etc. Also, they have been reported for various potential applications such as sensors [35–37], spintronics [38], field–effect transistor [36], spin–valve [39], and tunnel junction [40], etc.

Modifications in structural, microstructural, transport and magnetotransport properties in manganite based thin films have been discussed in the context of structural strain mainly due to the lattice mismatch between film and substrate [38,41–45]. Structural strain (at film–substrate interface) can be controlled by varying external parameters such as applied electric field [46], applied magnetic field [47], sintering temperature [48,49], annealing temperature [49], oxygen partial pressure for thin film [50], substrate for thin films [51], film thickness [52], swift heavy ion (SHI) irradiation [53], and fabrication route used [45], etc. SHI irradiation is one of the important tools (i) to create artificial defects in a lattice, (ii) to change the structural strain

\* Corresponding author.

E-mail address: [dhiren\\_pandya@yahoo.com](mailto:dhiren_pandya@yahoo.com) (D.D. Pandya).

and (iii) to modify the various physical properties of mixed valent manganite based thin films and devices [34,53–57]. Reports exist on transport and dielectric properties of manganite based thin films and devices under the SHI irradiation [34,53–57]. Ravalia et al. [34] have shown the irradiation-induced modifications in device characteristics of  $\text{La}_{0.6}\text{Pr}_{0.2}\text{Sr}_{0.2}\text{MnO}_3$  manganite films. It is also reported that temperature-dependent I–V characteristics performed across film–substrate interface and discussed in the context of defect formation and annealing effect [34]. Ravalia et al. [53] have fabricated the  $\text{La}_{0.8-x}\text{Pr}_{0.2}\text{Sr}_x\text{MnO}_3$  manganite films using PLD technique and studied the effect of 200 MeV  $\text{Ag}^{+15}$  ion irradiation on their transport properties. Udeshi et al. [54] have studied dielectric properties of PLD grown  $\text{NdMnO}_3$  manganite layer grown on LSAT substrate. They have discussed the effect of 200 MeV  $\text{Ag}^{+15}$  ion irradiation with different ion fluence on structural and electrical properties of  $\text{NdMnO}_3$  film. They have discussed the modifications in dielectric properties under the effect of SHI irradiation, mainly due to the role of grains and grain boundaries. Recently, Gadani et al. [55] have studied resistive switching (RS) behavior of PLD grown  $\text{Y}_{0.95}\text{Sr}_{0.05}\text{MnO}_3$  (YSMO) films on  $\text{Nb}: \text{SrTiO}_3$  (SNTO) substrate under the effect of 200 MeV  $\text{Ag}^{+15}$  ion irradiation. They have discussed RS behavior in the context of charge trapping–detrapping process and formation–rupture of filamentary conducting paths in the YSMO lattice. The device reproducibility and reliability for spintronic based applications have been studied through endurance behavior and retention ability measurement for pristine and all irradiated films. Also, RS behavior has been studied for the same (YSMO) films with different thickness ( $\sim 300$  nm) under the influence of 200 MeV  $\text{Ag}^{+15}$  ion irradiation by Hirpara et al. [56]. Recently, RS characteristics have been studied for YSMO films, deposited on a single crystalline Si substrate using PLD technique, by Rathod et al. [57]. In addition, they have reported the change in elemental compositions and the change in the oxidation state of Mn ions under the effect of 200 MeV  $\text{Ag}^{+15}$  ion irradiation through spectroscopy measurement for pristine and all irradiated films. Very few reports exist on the post annealing process studies, i.e. SHI irradiation on materials followed by annealing to annihilate the irradiation created defects in the materials lattice [58].

$\text{LaMnO}_3$  (LMO) is a parent compound in colossal magnetoresistance (CMR) family and one of the most interesting manganites with various interesting physical properties and, also, has different practical applications. Few reports are also available on structural, transport and electroresistance properties of  $\text{La}_{0.7}\text{Ca}_{0.3}\text{MnO}_3$  manganite based polycrystalline bulk [59], thin film [60] and nanoparticle [61]. Wu et al. [59] have studied the Electric-pulse-induced-resistance (EPIR) phenomenon and magnetic properties of  $\text{La}_{0.7}\text{Ca}_{0.3}\text{MnO}_3$  polycrystalline sample. They have discussed the resistive switching behavior by using the phase separation model with the percolation conduction mechanism. Vachhani et al. [60] have prepared  $\text{La}_{0.7}\text{Ca}_{0.3}\text{MnO}_3$  manganite based thin film and studied conduction mechanisms for the same. Dey et al. [61] have prepared  $\text{La}_{0.7}\text{Ca}_{0.3}\text{MnO}_3$  nanoparticles using sol-gel method and studied the effect of particle size on the transport and magnetotransport properties.

Present study focuses on the understanding of role of 100 MeV  $\text{O}^{+9}$  ions induced by SHI on structural, microstructural, and transport properties of  $\sim 100$  nm  $\text{La}_{0.5}\text{Gd}_{0.2}\text{Ca}_{0.3}\text{MnO}_3$  (LGCMO) films grown by PLD techniques. It is important to note that  $\text{Gd}^{+3}$  (rare-earth ion) has been selected as a partial substituted ion at A-site (i.e.  $\text{La}^{+3}$  site) mainly due to the smaller ionic radius of  $\text{Gd}^{+3}$  (1.107 Å for 9 coordination) than  $\text{La}^{+3}$  (1.21 Å 9 coordination), which results in a strong structural disorder at lattice and modifications in Mn–O–Mn bond angles. This aspect is directly reflected in structural, microstructural and transport properties of presently studied LGCMO manganite thin films. To understand the role of SHI irradiation, PLD grown LGCMO films were irradiated by 100 MeV  $\text{O}^{+9}$  ions using its different fluence. In depth structural, microstructural and transport studies have been performed for LGCMO–substrate p–n interface wherein the role of manganite defects (created through SHI irradiation experiment), in controlling the

conduction processes across manganite–substrate (p–n) interfaces has been discussed. These SHI induced defects of LGCMO manganites were annealed during the growth of  $\text{ZnO}$  thin (50 nm) layer, grown onto the surface of LGCMO layer for all pristine and irradiated films. This newly created CSD grown  $\text{ZnO}$ –LGCMO manganite p–n interfaces were again studied for change conduction mechanisms. Here, it is important to note that the defect nature of LGCMO–substrate p–n interface and  $\text{ZnO}$ –LGCMO p–n interface are completely different where for first case, LGCMO defects are created due to SHI irradiation whereas later case deals with annihilated (modified) LGCMO defects that have been studied in this communication.

## 2. Experimental details

A polycrystalline bulk sample of LGCMO manganite was synthesized by a conventional solid-state reaction (SSR) method [62]. Synthesis process includes mixing of high purity powders of lanthanum (III) oxide, gadolinium (III) oxide, calcium carbonate and manganese (IV) oxide taken in stoichiometric proportion, calcination at 600 °C for 6 h and grinding. Powdered sample was pelletized in the form of a disc (~20 mm diameter) using a hydraulic press. Final sintering of pellet was carried out at 1350 °C for 72 h. Well sintered pellet of LGCMO manganite was characterized by XRD measurement at room temperature using Cu K $\alpha$  radiation source to confirm its single-phase nature (XRD not shown here). Well sintered pellet was used as a target in the PLD technique to grow LGCMO films having ~100 nm film thickness on single crystalline (100)  $\text{Nb}: \text{SrTiO}_3$  (SNTO) substrates. 248 nm wavelength with fluence of ~200 mJ/cm<sup>2</sup> energy of KrF Excimer laser was used to ablate the target. Following parameters were employed: substrate temperature: ~750 °C, oxygen partial pressure: ~350 mT; target to substrate distance: ~5.5 cm, deposition time: 16 min for achieving 100 nm. To create artificial defects, all the LGCMO/SNTO films were irradiated by 100 MeV  $\text{O}^{+9}$  ions by different ion fluence using 15 UD Tandem Accelerator LGCMO films were irradiated with  $\sim 5 \times 10^{11}$ ,  $5 \times 10^{12}$  and  $5 \times 10^{13}$  ions/cm<sup>2</sup> that will be referred, hereafter, as LGCMO–11, LGCMO–12 and LGCMO–13, respectively. The pristine film will be named as LGCMO–PRI. To achieve homogenous ion irradiation on LGCMO films, ion beam was carefully scanned over the area (10 mm × 10 mm) of LGCMO film layers. Ion irradiation was performed perpendicular to the film plane. To estimate the projectile range as well as electronic energy loss ( $S_e$ ) and nuclear energy loss ( $S_n$ ), SRIM simulation program has been employed [63], as shown in Fig. 1a. According to SRIM simulation, values of all these three parameters are found to be ~0.69 keV/nm ( $S_e$ ), 0.38 eV/nm ( $S_n$ ) and 102.28 μm (projectile range). Comparatively larger projectile range suggests that ions can easily pass through the thin layers of LGCMO and penetrate into the substrate. This confirms that performed experiment is an ion irradiation, no implantation was taking place. Fig. 1b shows the damage profile (created using TRIM software) for present irradiation experiment with predicted almost 1000  $\text{O}^{+9}$  swift heavy ions that damaged the films having 100 nm film thickness. The structural and microstructural properties of pristine and irradiated LGCMO films were studied using XRD and AFM measurements, respectively, at room temperature. Room temperature I–V characteristics were performed using standard four-probe geometry under current perpendicular to plane (CPP) mode across LGCMO/SNTO p–n interfaces in the applied voltage range: –5 to +5 V, using computer-controlled Keithley 2612 A Source meter. Furthermore,  $\text{ZnO}$  thin layer with the thickness ~50 nm was grown on the surface of all the pristine and irradiated LGCMO films using CSD method by employing the following synthesis parameters and conditions: zinc acetate as starting material, double distilled water (DDW) and acetic acid (AA) in 1:1 vol ratio for solution preparation, desired yield: 0.3 M, stirring temperature: 90 °C, precursors solution: clean and transparent, spin coating speed: 4000 rpm, spin coating time: 25 s, calcination temperature and time: 300 °C for 30 min, annealing temperature and time: 700 °C for 12 h. Heating (cooling) rate: 5 °C/min (2 °C/min). After successfully grown  $\text{ZnO}$  thin

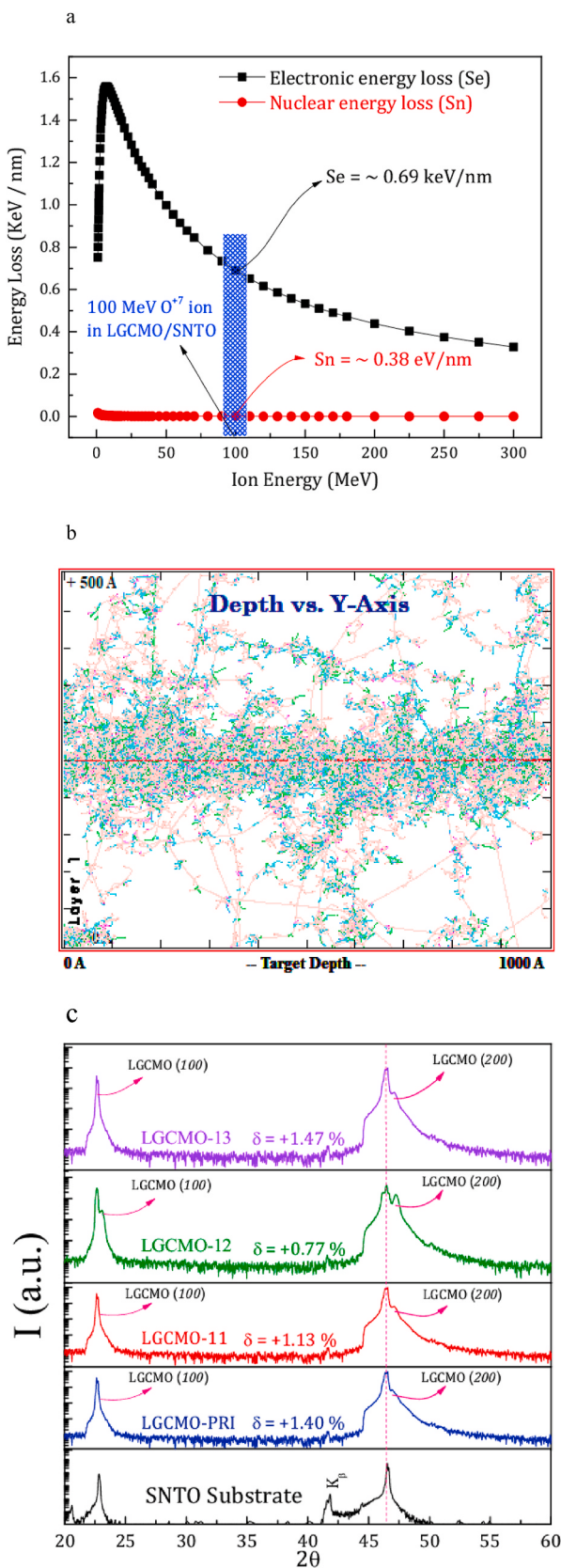


**Fig. 1.** (a) Electronic (Se) and Nuclear (Sn) energy loss spectra with ion energy, (b) damage profile exist for present SHI irradiation experiment and (c) XRD patterns of SNTO substrate and pristine and irradiated LGCMO/SNTO thin films.

layer, films will be referred, hereafter, as ZnO-11, ZnO-12, and ZnO-13 respectively. The pristine film will be named as ZnO-PRI. For these four samples, all the above measurements (i.e. XRD, AFM and I-V) have been performed at room temperature for ZnO-LGCMO interfaces. I-V measurements were performed across ZnO and LGCMO p-n interfaces using four-probe geometry. Four contacts of silver pad with the size of  $\sim 1 \text{ mm}^2$  were prepared for I-V measurements.

### 3. Results and discussion

**Fig. 1c** shows the XRD patterns of SNTO substrate, LGCMO-PRI, LGCMO-11, LGCMO-12 and LGCMO-13 manganites films. All the films possess single-phase nature without any detectable impurity and having orientation in  $(h00)$  direction parallel to substrate orientation. From XRD patterns, it is clearly seen that the peak position ( $2\theta$ ), as well as intensity of all the films, get modified with ion fluence of 100 MeV O<sup>+</sup>/ions. The peak separation between LGCMO film and SNTO substrate at  $\sim 46^\circ$  indicates the presence of structural strain ( $\delta$ ) at the interface (between LGCMO films and SNTO substrates) which can be calculated using the formula  $\delta (\%) = [(d_{\text{substrate}} - d_{\text{film}})/d_{\text{substrate}}] \times 100$ , where  $d_{\text{substrate}}$  and  $d_{\text{film}}$  are the lattice spacings for substrate and film, respectively. For the present case, all films possess tensile strain with its values found to be suppressed from PRI (+1.40%) to LGCMO-12 (+0.77%) and, finally, it gets enhanced in the higher ion fluence  $\sim 5 \times 10^{13}$  ions/cm<sup>2</sup>  $\sim +1.47\%$ . This can be attributed to the irradiation-induced modifications in the crystallinity of the films. From  $5 \times 10^{11}$  to  $5 \times 10^{12}$  ions/cm<sup>2</sup>, ion fluence enhances the number of defects in the material, which results in reduced crystallinity, while higher ion fluence, i.e.  $5 \times 10^{13}$  ions/cm<sup>2</sup> improves the crystallinity in the LGCMO lattice mainly due to local annealing in the LGCMO lattice.

An average crystallite size of the studied pristine and irradiated LGCMO/SNTO films can be calculated using the Scherrer's formula  $D = (K \times \lambda)/(\beta \times \cos\theta)$ , where  $D$  is an average crystallite size,  $K$  is dimensionless shape factor (0.9 for the present case),  $\lambda$  is the wavelength of the X-rays used,  $\beta$  is the line broadening of the XRD peak of LGCMO films. Estimated values of  $D$  are found to increase from 18.74 nm (LGCMO-PRI) to 22.93 nm (LGCMO-11) and 56.64 nm (LGCMO-12) with increase in ion fluence from pristine to  $5 \times 10^{11}$  to  $5 \times 10^{12}$  ion/cm<sup>2</sup>. For higher ion fluence,  $5 \times 10^{13}$  ion/cm<sup>2</sup>, an average crystallite size is found to be lowest  $\sim 15.29$  nm (LGCMO-13). Under the effect of SHI irradiation, crystallite size and, hence, crystallinity of the films has been modified as per ion fluence employed. But higher ion fluence of  $5 \times 10^{13}$  ion/cm<sup>2</sup>, maximum energy or heat gets produced and transferred to LGCMO-13 lattice that reduces the crystallite size and degrades the crystallinity (i.e. enhances the strain value).

**Fig. 2** shows the AFM images (2D images) with z-axis scale bar (top raw), surface (granular) profile (2nd raw) and average rms roughness analysis (3rd raw) for pristine and irradiated LGCMO/SNTO thin films. From the AFM images with z-axis scale bar (top), value of maximum height of the grain is found to be  $\sim 81.16$  nm (LGCMO-PRI), 31.14 nm (LGCMO-11), 28.79 nm (LGCMO-12) and 44.63 nm (LGCMO-13). Surface morphology has been modified under the effect of SHI irradiation with different ion fluence. This can be understood by using surface profile (2nd raw) and an average rms surface roughness analysis (3rd raw). Value of an average grain size increases from 84 nm (LGCMO-PRI) to 116.66 nm (LGCMO-12) while rms roughness decreases from 18.2 nm (LGCMO-PRI) to 4.9 nm (LGCMO-12) with an increase in ion fluence up to  $5 \times 10^{12}$  ions/cm<sup>2</sup>. For higher ion fluence, i.e.  $5 \times 10^{13}$  ion/cm<sup>2</sup>, an average grain size is found to decrease to  $\sim 66.66$  nm while rms surface roughness increases to  $\sim 19.2$  nm. This can be understood on the basis of irradiation effect as: with increase in ion fluence (from  $5 \times 10^{11}$  to  $5 \times 10^{12}$  ions/cm<sup>2</sup>), defects are created in the lattice thereby increase in defect density while for higher ions fluence, i.e.  $5 \times 10^{13}$  ions/cm<sup>2</sup>, recrystallization takes place due to huge amount of energy released within the LGCMO-13 lattice that reduces the defect density in the lattice of LGCMO-13.

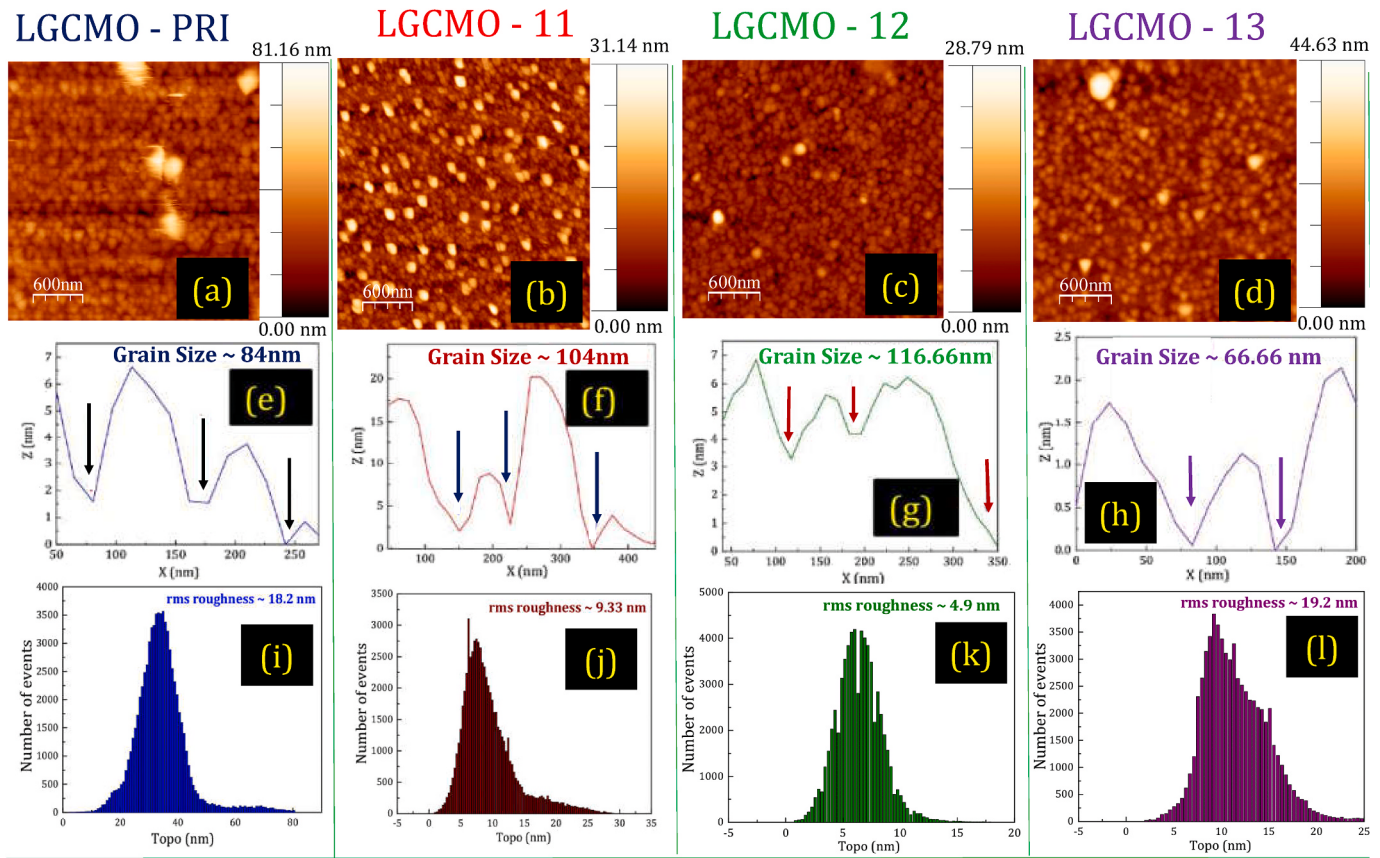


**Fig. 2.** AFM images (2D surface topography) with Z axis scale bar (a-d), surface (granular) profile with randomly selected grains (e-h) and average rms roughness analysis (i-l) of pristine and irradiated LGCMO/SNTO thin films along with the same scale bar of 600 nm ( $1 \times 1 \mu\text{m}$ ) for better comparison point of view.

Generally, grain size gets enhanced due to higher temperatures however for the present case of LGCMO films, due to local annealing effect, temperature of the lattice gets enhanced considerably. As a result of this recrystallization takes place which, finally, consequences in the formation of new lattice of LGCMO-13 film. In this case, mostly it is possible to achieve an improved crystal state of any film through recrystallization process (due to higher temperature created within the lattice and huge amount of energy released by higher fluence SHI irradiation). Although one cannot ignore the possibility of non-reverse process of crystallization and final crystal state (after recrystallization) becomes poor in condition, as compared to initial one (i.e. before irradiation or recrystallization). Present case of LGCMO-13 film follows the later effect and recrystallization degrades the crystallinity of the film under high ion fluence thereby grain size gets suppressed, strain gets enhanced and crystallite size gets reduced for this LGCMO-13 film. In addition, strain in the films also depends on the average grain size through the microstrain and coexisting strain regions based aspects. This can be understood as: grains are consisting of grain cores and grain boundaries. Grain cores are more crystalline in nature with less possible number of defects within its lattice whereas grain boundaries possess more number of defects and imperfections within its own lattice. As a result, one can expect better matching between the crystal lattice of grain cores and substrate used however considerable mismatch can be expected from the lattice mismatch between the granular boundaries and substrate lattice. In this point of view, films having larger grain sizes and lower grain boundary density possess smaller lattice mismatch and crystalline strain between the film and substrate whereas the films with smaller grain sizes and larger grain boundary density possess higher lattice mismatch and crystalline strain between the film and substrate lattice. This case of correlations between the strain values and grain sizes can be observed from the presently studied LGCMO/SNTO thin film

devices wherein the strain gets suppressed from pristine to  $5 \times 10^{12}$  ions/cm<sup>2</sup> irradiation fluence based film and grain size gets enhanced from pristine to  $5 \times 10^{12}$  ions/cm<sup>2</sup> irradiation fluence based film. However, suppressed value of grain size in higher studied ion fluence based LGCMO/SNTO film gets suppressed with a marginally enhanced strain value.

To understand the transport properties across LGCMO-SNTO p-n interfaces (at room temperature) for presently studied pristine and all irradiated films, current-voltage (I-V) was carried out using four-probe method. Fig. 3 shows the I-V curve of pristine LGCMO film for applied voltage between +5 and -5 V across LGCMO-SNTO interface. Inset shows the geometry used for I-V characteristics performed for the present case. It is clearly seen that pristine p-n interface exhibits nonlinear nature of the I-V curve along with backward diode characteristics, i.e. value of reverse current is larger as compared to forward current ( $I_R > I_F$ ) [41]. In forward bias mode, electrons of SNTO substrate get sufficient energy and start to overcome the depletion region between LGCMO film and SNTO substrate and flow towards LCGMO film. This results in the conduction across the interface along with the critical voltage ( $V_C$ )  $\sim 0.5$  V (from where the considerable current starts to increase during forwarding bias mode; Fig. 3). During the reverse bias mode, applied negative voltage enhances the width of the depletion region across LGCMO-SNTO p-n interface. This depletion region (junction) can be considered as an insulating region. Therefore, charge carriers (number of charges) are not able to cross over the interface up to  $\sim -1$  V (which is called critical voltage  $V_C$  in the reverse bias mode). After getting sufficient energy from applied negative voltage, charge carriers continue to flow through the interface and increase in current with an applied negative voltage can be observed and, also, reach to its maximum  $\sim -2.6$  mA at -5 V. Observed larger reverse ( $I_R$ ) current as compared to forward ( $I_F$ ) current is known as backward diode-like behavior ( $I_R > I_F$ ).

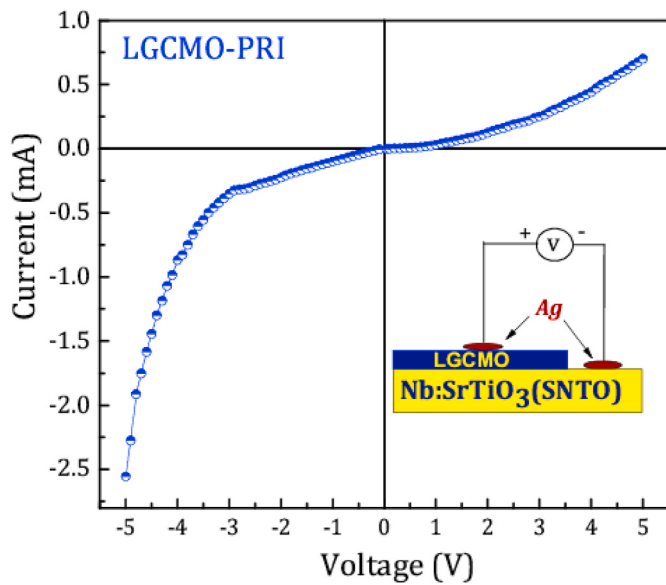


**Fig. 3.** I–V curve of pristine LGCMO film, applied voltage  $-5$  to  $+5$  across LGCMO – SNTO interface. Inset shows the geometry used for I–V characteristics performed for the present case.

Backward diode-like characteristics have been observed for the presently studied pristine LGCMO/SNTO film. To understand the backward diode-like behavior or origin of backward diode-like characteristics, three mechanisms can be considered: (i) tunneling effect between two oxide layers (LGCMO/SNTO), (ii) thermal excitation and (iii) leakage processes [64,65]. The tunneling effect depends upon the thickness of the depletion region, (ii) thermal excitation depends on the height of the barrier and (iii) leakage processes depend on imperfection/disorder

such as defects, vacancies, pinholes, etc in the interface region. For the present case, tunneling effect becomes possible under the reverse bias mode, across LGCMO/SNTO p–n interface. Width of the depletion region gets enhanced during the reverse bias mode therefore the movement of charge carriers from LGCMO film to SNTO substrate becomes difficult during  $0$  to  $-3.5$  V. Hence, obtained lower conduction (between  $-0.5$  mA @  $-3.5$  V) across LGCMO/SNTO p–n interface (Fig. 3) can be observed however above  $-3.5$  V, charge carriers get sufficient energy to break the depletion region and sharp increase in current (between  $-2.6$  mA @  $-5$ V) via tunneling mechanism could be recorded. For the present study, the strong structural disorder has been observed due to structurally dissimilarity between LGCMO (orthorhombic) and SNTO (cubic) therefore one can expect a small barrier height across the interface between LGCMO and SNTO which allows thermal excitation process across the interface that contributes to backward diode character efficiently, as observed in Fig. 3. Last possibility, leakage current also becomes one of the major sources of backward diode character since presence of defects, vacancies, pinholes and other imperfections can be expected SNTO across the LGCMO and interface [66].

Fig. 4 shows the variation in interface current between the pristine and irradiated LGCMO manganite films and SNTO substrates recorded under variation in applied voltage between  $-5$  and  $+5$  V for (a) LGCMO-PRI, (b) LGCMO-11, (c) LGCMO-12 and (d) LGCMO-13. All the films display completely distinguishable I–V characteristics at room temperature indicates that irradiation effectively modifies the transport across the interfaces under study. One can realize that current in the forward bias mode increases from LGCMO-PRI film to LGCMO-11 film and LGCMO-12 film which can be understood as: (i) as shown in Fig. 1, lattice strain gets suppressed from  $+1.40\%$  (LGCMO-PRI) to  $+1.13\%$  (LGCMO-11) and  $+0.77\%$  (LGCMO-12). As a result, transport across the interface becomes easier with increase in ion fluence up to  $5 \times 10^{12}$  ions/cm<sup>2</sup> [20,45,49]. This is due to fact that interface contains more structural disorder and structural defects between the film and substrate

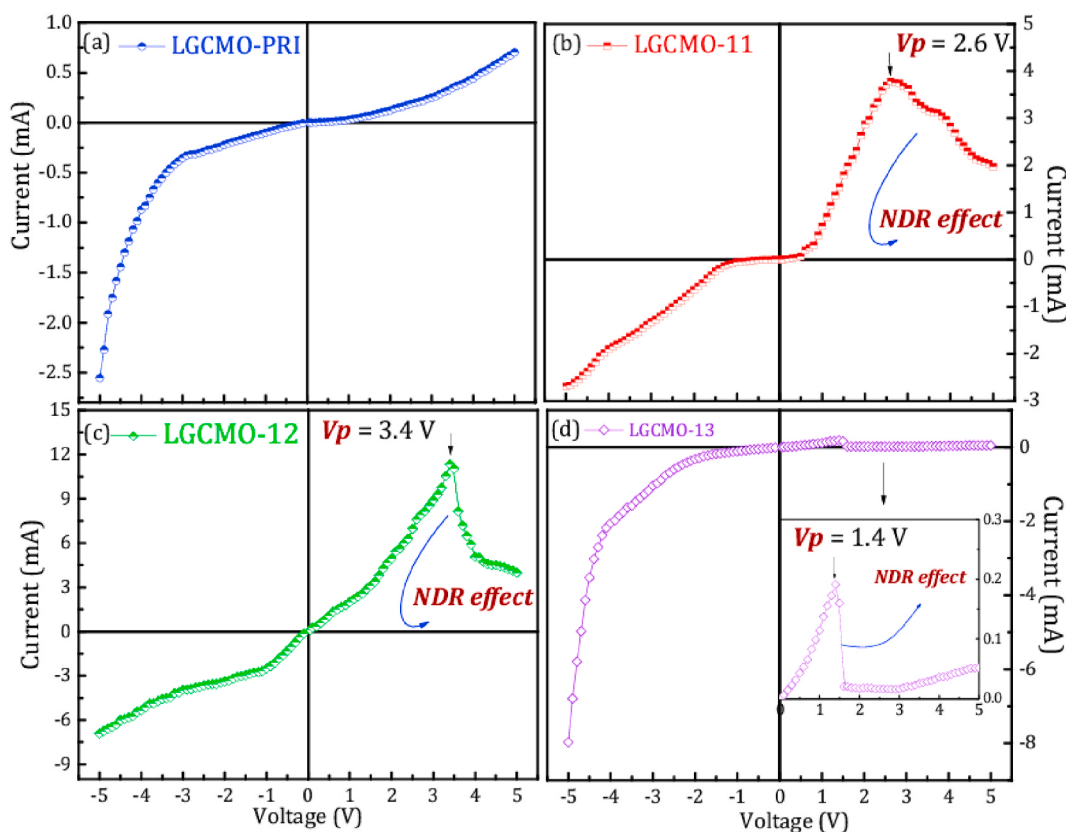


**Fig. 4.** I–V characteristics of (a) LGCMO-PRI, (b) LGCMO-11, (c) LGCMO-12 and (d) LGCMO-13 at room temperature.

that controls the conduction across it, (ii) as shown in Fig. 2, an average grain size increases from pristine film to  $5 \times 10^{11}$  ions/cm<sup>2</sup> fluence irradiated manganite film followed by further increase in an average grain size in  $5 \times 10^{12}$  ions/cm<sup>2</sup> fluence irradiated manganite film. This results in the reduction in total number of grain boundaries in the higher fluence (up to  $5 \times 10^{12}$  ions/cm<sup>2</sup>) irradiated manganite films. Conduction across the manganite films gets controlled by the high resistive nature of the grain boundaries that provide larger resistance to the films having smaller grain size [20,45,49]. In this regard, pristine film exhibits larger resistance and smaller value of interface current as compared to  $5 \times 10^{11}$  ions/cm<sup>2</sup> and  $5 \times 10^{12}$  ions/cm<sup>2</sup> fluence irradiated films, (iii) existence form of grains and grain boundaries can be considered as phase separation scenario in the presently studied LGCMO manganite films. This can be expected because grains are low resistive metallic in nature whereas grain boundaries are high resistive (comparative to grains) insulating in nature and both grains and grain boundaries are present in the films' single phase. From pristine to  $5 \times 10^{12}$  ions/cm<sup>2</sup> fluence irradiated film, low resistive grain content gets enhanced and grain boundary density gets suppressed thereby our current observed across film substrate interface is increased, as shown in Fig. 4. For higher fluence, forward current gets efficiently reduced, as shown in Fig. 4d. This can be understood in terms of enhanced structural strain between the film and substrate ( $\sim +1.47\%$ ; Fig. 1c). Due to enhanced structural strain, charge conduction across the interface becomes difficult thereby recorded current gets suppressed. In addition, as shown in Fig. 2, upon irradiation using higher ion fluence (i.e.  $5 \times 10^{12}$  ions/cm<sup>2</sup>), grain size gets reduced whereas grain boundary density gets enhanced. As a result, charge conduction across the film lattice is controlled through the high resistive grain boundaries. This provides larger interface resistance and smaller recorded current as shown in Fig. 4d. Effect of SHI irradiation (ion fluence) on the reverse current values will be discussed in the following section.

Studied LGCMO-11 film exhibits an increase in current with increasing voltage up to  $\sim 2.6$  V (which is indicated as  $V_p$ ) after which current starts to decrease up to the studied voltage range (i.e.  $+5$  V) in the forward bias region. This indicates that after  $\sim 2.6$  V, LGCMO-11 film interface exhibits negative differential resistance (NDR) behavior. In manganites, NDR behavior can be understood on the basis of possible phase separation scenario exists in the presently studied manganite films. Since, presently studied manganite films are insulating in nature at room temperature, insulating phase is dominating metallic phase in the films lattices. In other words, all films are not fully insulating in nature but they are phase coexisting materials consist of metallic and insulating clusters. In this, insulating clusters are dominating metallic one thereby films behave as insulators at room temperature. This can be expected due to fact that La<sub>0.7</sub>Ca<sub>0.3</sub>MnO<sub>3</sub> manganite exhibits metal to insulator phase transition temperature near 270K (well below room temperature) [49]. Upon addition of 20% Gd<sup>+3</sup> ions at La<sup>+3</sup> site in La<sub>0.7</sub>Ca<sub>0.3</sub>MnO<sub>3</sub>, i.e. LGCMO, overall transport gets suppressed due to structural disorder and size variance effect [45]. As a result, electronic phase transition temperature gets, further, reduced towards lower temperature, even lower than 270K. In this context, LGCMO manganite is also believed to be insulating in nature at room temperature. Upon increase in applied voltage, current gets enhanced monotonically up to  $V_p \sim 2.6$  V. Well above  $\sim 2.6$  V applied voltage, sufficient joule heating is created within the insulating LGCMO manganite that generates local heating in the lattice thereby LGCMO manganite becomes more insulating in nature. This controls the current to pass across its lattice which provides reduction in current with further increase in applied voltage well above  $\sim 2.6$  V, as shown in Fig. 4b.

Upon further increase in ion fluence up to  $5 \times 10^{12}$  ions/cm<sup>2</sup>, i.e. LGCMO-12 film, current gets enhanced with applied voltage up to  $\sim 3.4$  V above which current is found to decrease sharply with further increase in applied voltage. This voltage peak,  $V_p$ , can be understood on the basis of joule heating based increase in local temperature within the lattice of LGCMO-12 film. As a result of the same, LGCMO-12 film becomes less

insulating (as compared to LGCMO-11 film) in nature followed by reduction in current well above  $\sim 3.4$  V applied voltage. It is interesting to note that  $V_p$  is reduced from LGCMO-12 to LGCMO-11 film which may be attributed to the fact that LGCMO-12 film is more conducting in nature that creates less joule heating and lower local temperature within the LGCMO-12 film lattice as compared to LGCMO-11 film lattice. As a consequence of the same,  $V_p$  shifts towards lower temperature, since larger voltage induced joule heating is required to control the conduction, i.e. current, across the lattice of LGCMO-12. For higher ion fluence studied in the present case for LGCMO-13 film, presence of  $V_p$  can be realized at lower applied voltage  $\sim 1.4$  V. Reduction in  $V_p$  can be attributed to the lowest observed conduction within this lattice due to higher rms surface roughness, lower structural strain and smaller grain size, as a result of which conduction becomes difficult within the lattice. As a consequence, largest joule heating and local temperature can be expected for LGCMO-13 film lattice that controls the current across it at lower applied voltage thereby  $V_p$  gets suppressed to  $\sim 1.4$  V in Fig. 4d.

As shown in Fig. 4a, reverse current is larger than forward current that justifies the backward diode character of the LGCMO-PRI film. This has already been discussed in the context of tunneling process between LGCMO manganite thin layer and SNTO substrate, thermal excitation induced movements of charge carriers across the interface between LGCMO and SNTO and leakage current induced enhancement in reverse current for LGCMO-PRI film. Upon irradiation using  $5 \times 10^{11}$  ions/cm<sup>2</sup> fluence, lattice strain gets suppressed from 1.40% (in pristine film) to 1.13% in LGCMO-11 film. Reduction in strain across the interface between LGCMO manganite layer and SNTO substrates for the case of LGCMO-11 film provides reduced insulating thin layer (i.e. strained region) that suppresses the possibility of tunneling across the interface between LGCMO and SNTO in LGCMO-11 film thereby controls the contribution to reverse current and, hence, backward diode character in this film. Since structurally disordered high resistive strained region gets suppressed in LGCMO-11 film, it cannot provide sufficiently larger thermal excitations for the charge carriers thereby cannot contribute effectively to reverse current and, hence, backward diode character in LGCMO-11 film. One can also observe no leakage current across the interface thereby it cannot provide backward diode nature. As a consequence of all these, backward diode nature is absent in LGCMO-11 film, as shown in Fig. 4b. With increase in higher ion fluence up to  $5 \times 10^{12}$  ions/cm<sup>2</sup> in LGCMO-12 film, no backward diode character can be realized, similar to LGCMO-11 film which can be ascribed to the reduced lattice strain value thereby no possibility of tunneling induced enhancement in reverse current as well as thermal excitation induced conduction improvement during reverse bias mode. However, small contribution can be expected from leakage current induced enhancement in reverse bias current, as shown in Fig. 4c. This contribution gets overcome by depletion region supported control of current across the interface thereby overall no backward diode signature can be observed for LGCMO-12 film. For higher fluence irradiated LGCMO-13 film, one can consider the causes for observed backward diode characteristics as: (i) tunneling process between conducting LGCMO manganite oxide and semiconducting SNTO substrate with intermediate thin layer of high resistive stained region, due to larger strain value  $\sim 1.47\%$ , (ii) presence of higher strained region between LGCMO-13 and SNTO oxides, thermal excitations become possible that contribute effectively to reverse current value thereby backward diode character and (iii) negligibly small leakage current also adds fraction of reverse current to support the backward diode characteristics across LGCMO/SNTO manganite interface irradiated at higher ion fluence of  $5 \times 10^{13}$  ions/cm<sup>2</sup>. In the present case of LGCMO-13 film, highest value of strain state  $\sim 1.47\%$  has been observed (among all four thin film based interfaces) that provides highest tunneling and thermal excitations thereby strongest backward diode characteristic can be observed in Fig. 4d.

ZnO 50 nm thick film (layer) was grown over the surfaces of LGCMO pristine and irradiated films using low cost CSD method followed by complete bilayered devices' annealing under oxygen environment.

Annealing process on ZnO/LGCMO/SNTO bilayered devices was performed for the same time, same temperature and same environment, i.e. speed of flow of oxygen gas. Annealing process can annihilate the defect states of the LGCMO manganite films, however original defect states (similar to LGCMO-PRI film) cannot be obtained back thereby some defects remain in the lattice even after annealing process. Different ion fluence based LGCMO manganite films possess different microstructure even after annealing process which make a strong effect of their microstructure and structure on the similar I-V characteristics, recorded at room temperature for ZnO/LGCMO interface. To understand the role of modified structure and microstructure on the charge transport properties, I-V characteristic was recorded for all the films after annealing process performed across the ZnO/LGCMO interfaces.

Fig. 5 shows the XRD patterns of all ZnO/LGCMO/SNTO bilayered thin film devices (after annealing process) which clearly reveal the single-phase nature of ZnO layers (for all four devices) and LGCMO films with  $(h00)$  crystallographic orientations, i.e. parallel to substrate orientations, along with the lattice mismatch between annihilated LGCMO films and SNTO substrates. In addition, the peak position ( $2\theta$ ) and intensity have been modified from ZnO-PRI to ZnO-13 film. The lattice mismatch can be estimated by using the formula:  $\delta (\%) = [(d_{\text{substrate}} - d_{\text{film}})/d_{\text{substrate}}] \times 100$ , where  $d_{\text{substrate}}$  and  $d_{\text{film}}$  are the values of  $d$ -spacing for substrate and film, respectively. The positive and negative value of  $\delta$  represented to tensile or compressive strain, respectively. Presently studied LGCMO/SNTO interface possess tensile strain with its positive value ( $\delta$ ) that gets suppressed from ZnO-PRI (+2.62%) to ZnO-12 (+1.43%) while reduced more effectively for ZnO-13 film (+0.84%). This can be attributed to the annihilation effect which can provide a sharp interface, i.e. improved strain between films and substrates. In other words, irradiated LGCMO/SNTO films (with ion fluence up to  $5 \times 10^{12}$  ions/cm $^2$ ) possess lower values of lattice strain as compared to annihilated irradiated LGCMO/SNTO films (with ion fluence up to  $5 \times 10^{12}$  ions/cm $^2$ ) which can be ascribed to the fact that annihilation process eliminates the defects/oxygen vacancies (by filling up the oxygen vacancies through a flow of oxygen during annealing) near the interface between LGCMO films and SNTO substrates. As a result, the strain between films and substrates gets suppressed and interface becomes more crystalline and effectively sharp in nature. The

case of higher studied ion fluence of  $5 \times 10^{13}$  ions/cm $^2$  can be understood as: when annealing is provided to the ZnO-13 film, this annihilation will provide more temperature to the lattice. However, this lattice of LGCMO-13 has already experienced a recrystallization during irradiation process (i.e. LGCMO-13) and, hence, its strain gets enhanced for LGCMO-13 film (Fig. 1c). Due to post annealing process (where LGCMO-13 film is, now, known as ZnO-13 film after annealing process), ZnO-13 film experienced the improvement in the crystalline structure thereby strain gets suppressed in ZnO-13 (from LGCMO-13 film) and granular morphology gets improved. Also, the observed XRD peaks at  $20 \sim 36^\circ$  and  $\sim 55^\circ$  correspond to the  $(002)$  and  $(110)$  ZnO orientations, respectively, suggesting the polycrystalline growth of the ZnO layer (indicated by symbol \*) on LGCMO/SNTO devices. A similar observation was reported by Polek et al. [67] in ion-beam sputtering grown ZnO layer ( $\sim 50$  nm)/LBMO film on SrTiO<sub>3</sub> (STO) substrate. In addition, intensity of XRD peaks (ZnO layer) gets suppressed from ZnO-PRI to ZnO-13. This can be ascribed to the intermediate process between well irradiated followed by annihilated LGCMO films (having different defect densities) and very sharp ( $\sim 50$  nm) ZnO layer. This process is directly reflected in surface morphology of ZnO layer in the form of grain size and surface roughness.

Fig. 6 shows the AFM images (2D) with Z-axis scale bar (top raw/1st raw), surface (granular) profile (2nd Raw) and average rms roughness analysis (3rd raw) for LGCMO layers after the growth of ZnO layer and after providing annealing process. All the AFM images (2D) have been recorded at the same scale bar of 1200 nm for better comparison purpose. All the films possess an island-like granular surface structure. It can be revealed that microstructure of all LGCMO manganite layers get altered effectively due to annealing under oxygen environment with remarkable modifications in the grain growth processes. ZnO-PRI possesses an average grain size  $\sim 116$  nm which gets effectively enhanced to  $\sim 134$  nm and  $\sim 212$  nm for ZnO-11 and ZnO-12 film, respectively. This may be ascribed to the better growth of granular structure in LGCMO manganite having a larger grain sizes after SHI irradiation. In other words, if LGCMO/SNTO film possesses larger grain size after SHI irradiation, post annealing process provides annihilation effect thereby grains get agglomerated and become larger after annealing (Fig. 6) as compared to their initial grain size (Fig. 2), for each studied device. Larger fluence based LGCMO/SNTO film, after annealing, also possesses larger grain size  $\sim 84$  nm than its grain size before annealing (i.e.  $\sim 66.66$  nm). However,  $\sim 84$  nm grain size possesses by LGCMO manganite thin layer after annealing process (i.e. ZnO-13) is lower than other lower fluence based annealed LGCMO films (i.e. ZnO-PRI, ZnO-11 and ZnO-12). From ZnO-PRI to ZnO-12, rms surface roughness gets suppressed whereas for ZnO-13 film, rms surface roughness gets enhanced, as shown in Fig. 6 (lower, 3rd, raw).

In order to understand the correlations between the structure and microstructure of annihilated LGCMO manganite films in ZnO/LGCMO/SNTO devices with transport properties and charge conduction across LGCMO manganite thin layers (pristine and irradiated after annealing process), I-V characteristic was performed across ZnO/LGCMO interfaces (after annealing process) at room temperature. Fig. 7 shows the I-V characteristics of ZnO/LGCMO interface after annealing process (for pristine LGCMO layer), i.e. ZnO-PRI film. Measurement geometry is shown in the inset of Fig. 7 where almost negligible current is drawn across ZnO/LGCMO (annihilated pristine) interface. This can be attributed to the smaller grain size of LGCMO (annihilated pristine) film, as compared to other annihilated irradiated films, in which large number of grain boundaries are present. These grain boundaries are comparatively high resistive in nature due to disorder, present in this region. This can also be ascribed to the larger strained region between LGCMO (annihilated pristine film) and SNTO substrate. However, current was recorded for ZnO/LGCMO interfaces, strain between LGCMO (annihilated pristine and irradiated) films and SNTO substrates inserts the disorder in the entire thin film/layer of LGCMO manganite hence strain at LGCMO/SNTO interfaces also affect largely the current across ZnO/

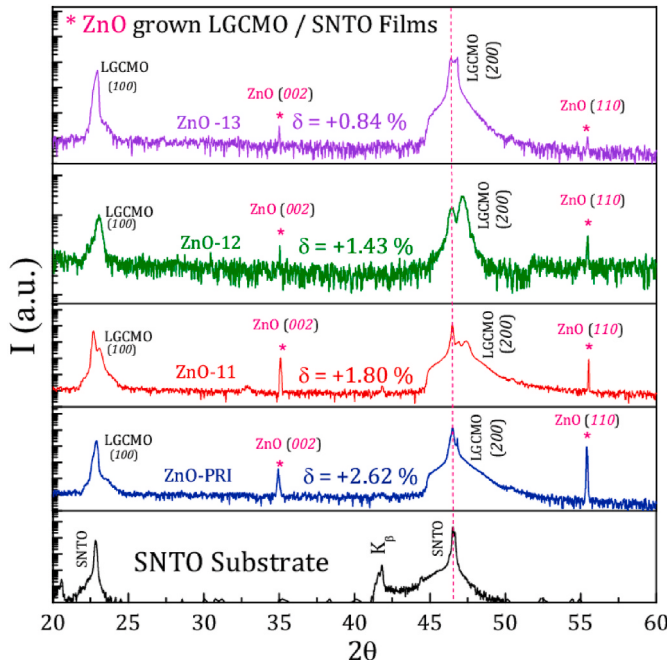
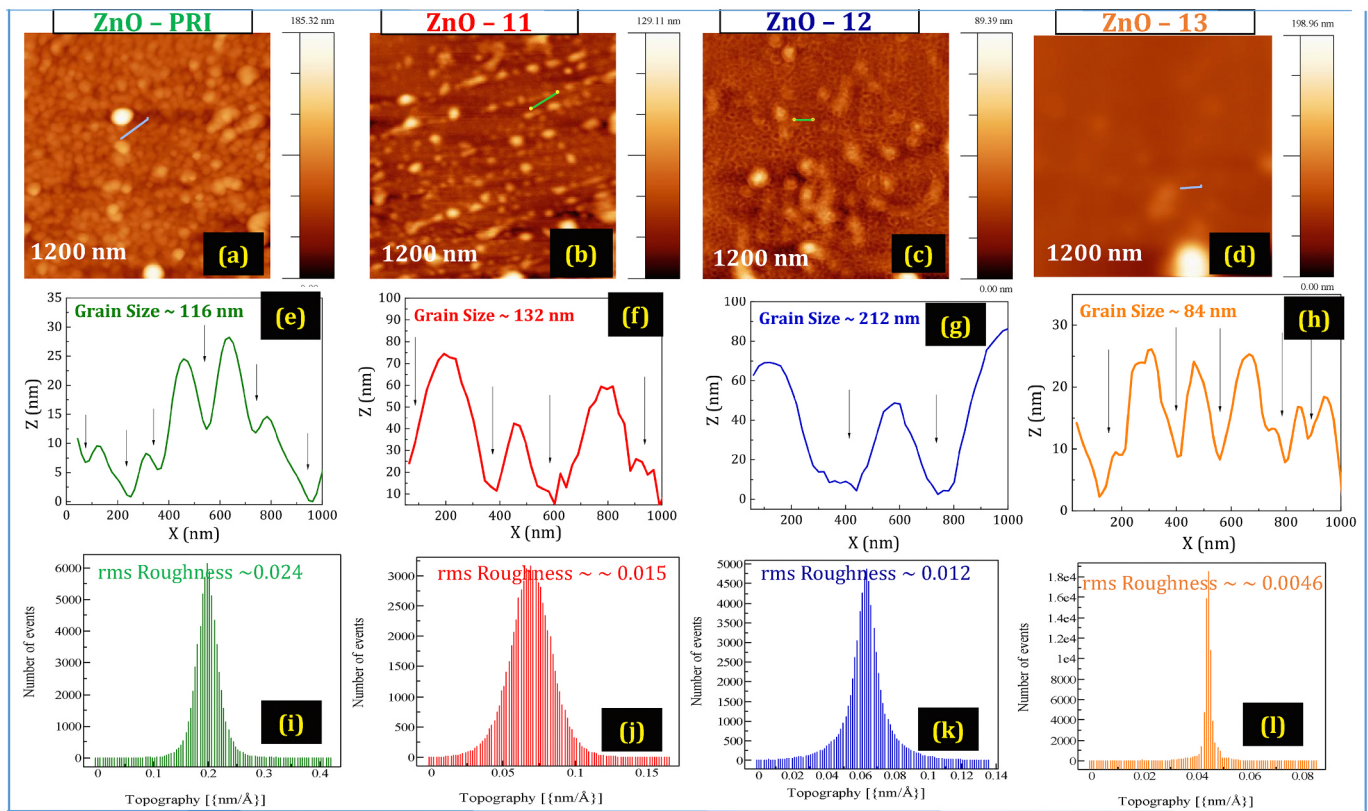
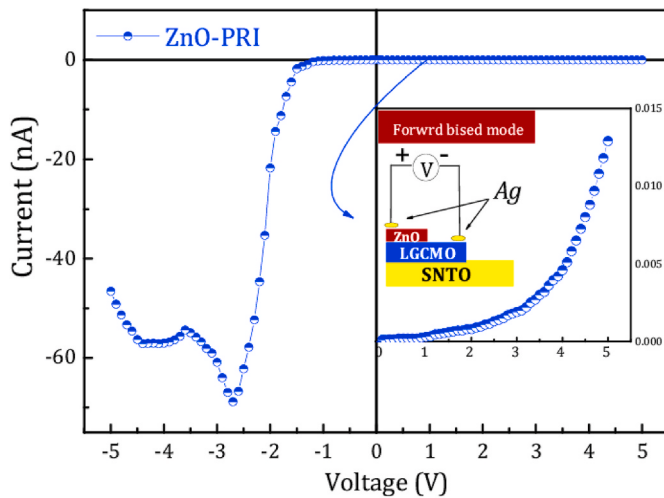


Fig. 5. XRD patterns of SNTO substrate and ZnO thin layer grown LGCMO pristine and irradiated films.



**Fig. 6.** AFM images (2D surface topography) with Z-axis scale bar (a-d), surface (granular) profile with randomly selected grains (e-h) and average rms roughness analysis (i-l) of LGCMO pristine and irradiated thin films along with the same scale bar of 1200 nm ( $1 \times 1 \mu\text{m}$ ) for better comparison point of view.



**Fig. 7.** I-V curve of pristine ZnO/LGCMO/SNTO film, applied voltage  $-5$  to  $+5$  across ZnO-LGCMO interface. Inset shows the geometry used for I-V characteristics performed for the present case.

LGCMO interfaces for all four devices under study. For reverse bias mode, one can observe comparatively large current across the ZnO/LGCMO interface in ZnO-PRI device which can be ascribed to the backward diode characteristics. This can also be attributed to the thermal excitations and large leakage current across the ZnO/LGCMO interface observed during reverse bias mode. However, tunneling cannot be possible due to poor barrier between the ZnO oxide and LGCMO manganite layers. One can expect poor barrier between the two because ZnO has been grown using CSD method followed by annealing

under oxygen environment and, hence, interface becomes much disordered in nature thereby poor barrier exists between them. Across this poor barrier, no sharp tunneling layer can be expected that's why tunneling process induced increase in current during reverse bias mode cannot be considered as a cause for backward diode characteristic. In reverse bias mode, one can also observe the tunnel diode characteristics in which current gets suppressed after a  $\sim -2.8$  V applied voltage followed by again increase in reverse current after  $\sim -3.6$  V and second reduction in current at  $\sim -4.35$  V. Presence of double  $V_p$  values during reverse bias mode can be ascribed to high disordered interface between LGCMO (annihilated pristine film) and SNTO with larger strain  $\sim 2.62\%$ .

Fig. 8 shows the variation in current across ZnO/LGCMO manganite interfaces for (a) ZnO-PRI (i.e. annihilated pristine LGCMO case), (b) ZnO-11 (i.e. annihilated irradiated LGCMO case with  $5 \times 10^{11}$  ions/cm $^2$ ), (c) ZnO-12 (i.e. annihilated irradiated LGCMO case with  $5 \times 10^{12}$  ions/cm $^2$ ), and (d) ZnO-13 (i.e. annihilated irradiated LGCMO case with  $5 \times 10^{13}$  ions/cm $^2$ ) devices. Upon increase in ion fluence to  $5 \times 10^{11}$  ions/cm $^2$  (annihilated irradiated film) in ZnO-11 film, current across ZnO/LGCMO interface gets enhanced effectively. This can be ascribed to the enhanced grain size of LGCMO manganite layer after annealing as well as suppressed strain state between LGCMO annihilated pristine film and SNTO substrate in ZnO-11 device. Improved grain size results in the reduced number of grain boundaries which are high resistive in nature. As a consequence, current across ZnO and LGCMO interface gets enhanced largely during forward bias mode [Fig. 8b]. During its reverse bias mode, large leakage has been observed, as shown in Fig. 8b that contributes large enough current across the interface between ZnO and LGCMO thin layers. However, no backward diode characteristic is obtained for the case of ZnO-11 film. Absence of backward diode character can be ascribed to the larger grain size induced improved forward bias current as well as absence of strong barrier between ZnO and LGCMO layers. Further increase in SHI irradiation fluence in ZnO-12 device, ZnO/LGCMO interface allows larger current across it which can be

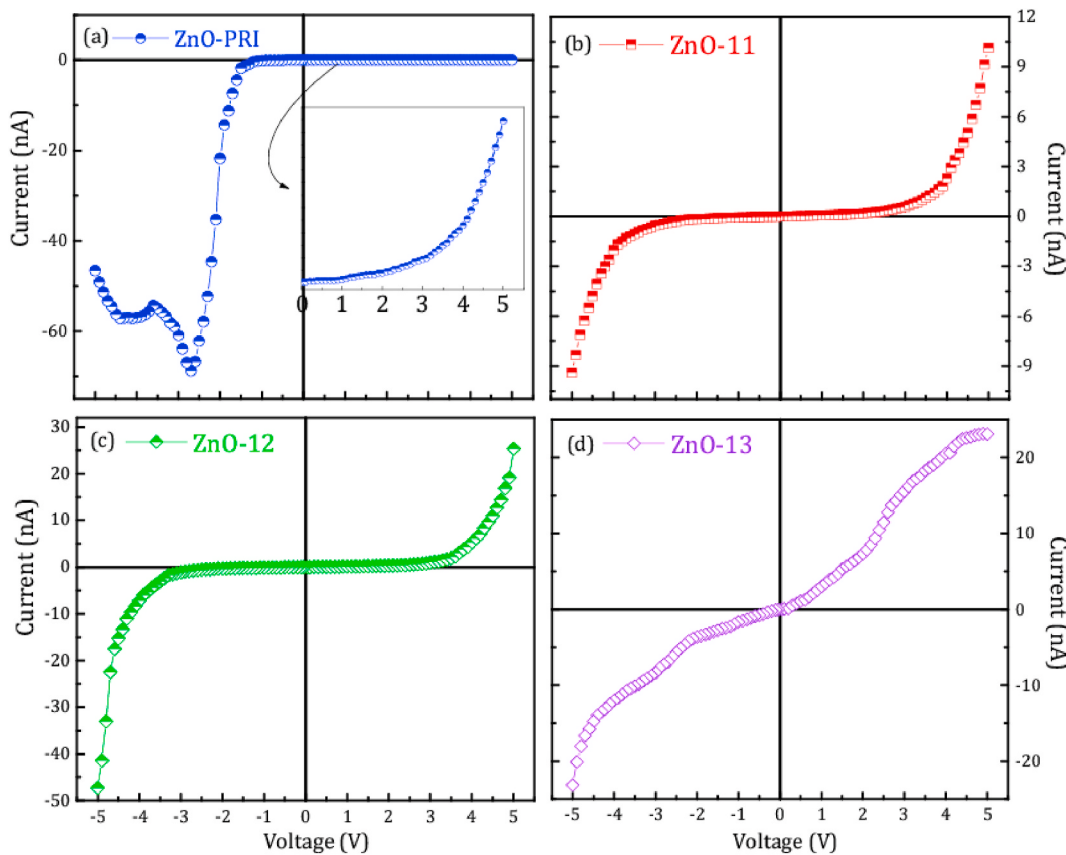


**Fig. 8.** I-V characteristics of (a) ZnO-PRI, (b) ZnO-11, (c) ZnO-12 and (d) ZnO-13 at room temperature.

attributed to the improved grain size, reduced grain boundary density and, also, contribution from further reduced strain state between LGCMO and SNTO (after annealing of  $5 \times 10^{12}$  ions/cm<sup>2</sup> irradiated film). Contribution from reduced strain between LGCMO and SNTO materials can be considered for forward current enhancement due to fact that reduced strain inserts comparatively lower disorder in the manganite layer thereby supports more the current across the same, as shown in Fig. 8c during forward bias mode. During its reverse bias mode, backward diode characteristics can be observed wherein current during reverse bias mode becomes larger than forward bias mode based current. This becomes again possible due to larger leakage current (up to  $\sim -3$  V) across the ZnO/LGCMO interface. This leakage current becomes highest among all four studied ZnO/LGCMO/SNTO devices where one can realize presence of a strong backward diode character at room temperature. Further increase in SHI irradiation dose of ions to  $5 \times 10^{13}$  ions/cm<sup>2</sup>, i.e. ZnO-13 device, wherein LGCMO manganite layer is irradiated using this higher fluence followed by its annealing under oxygen environment. In this film, LGCMO manganite layer possesses lower grain size with large number of high resistive grain boundaries thereby it allows reduced current across it during forward bias mode. For forward bias mode, no backward diode character can be observed, like ZnO-11 film, which can be due to absence of any leakage current across the interface during reverse bias mode. Overall complex charge transport mechanisms and related processes can be understood on the bases of strain state between LGCMO manganite layers and SNTO substrates before annealing and after annealing process (i.e. annihilated states).

#### 4. Conclusion

In this communication, we report the results of the studies on the effect of 100 MeV O<sup>+7</sup> ion irradiation in modifying structural (lattice

strain), surface morphology and I-V characteristics of PLD grown LGCMO manganite films on single crystalline SNTO substrate. Decrease in the structural lattice strain has been observed up to a fluence of  $5 \times 10^{12}$  ion/cm<sup>2</sup> and improvement in the grain size results in an enhancement in conduction (I-V) across LGCMO-SNTO interface while for higher ion fluence, i.e.  $5 \times 10^{13}$  ions/cm<sup>2</sup> conduction across p-n interface gets suppressed due to suppressed grain size with increased grain boundary density as well as rms surface roughness in the LGCMO lattice. I-V characteristics also show that all the films exhibit non-linear (I-V curves) behaviors which have been discussed in the context of lattice strain, grain size and grain boundary density. LGCMO-PRI film exhibits backward diode like behavior while irradiated films (LGCMO-11 & LGCMO-12) possess tunnel diode like behavior. These I-V behaviors (i.e. backward diode and tunnel diode characters) of LGCMO/SNTO p-n interfaces have been discussed in detail. To achieve annihilation effect through successful growth of 50 nm thick ZnO layer over the surfaces of each studied LGCMO/SNTO thin films using CSD method, growth was performed under controlled flow of oxygen flow. XRD patterns (recorded after annihilation) reveal the single phase polycrystalline growth of ZnO layer over the LGCMO/SNTO thin films' surfaces. Positive value of tensile strain across LGCMO/SNTO interface gets suppressed under the ion fluence, i.e. ( $5 \times 10^{11}$  to  $5 \times 10^{13}$  ion/cm<sup>2</sup>) due to the annihilation effect which can provide a sharp interface. The effect of annihilation on the surface morphology of ZnO/LGCMO/SNTO films was studied by performing AFM measurement. Average grain size, from AFM images, is found to increase in ion fluence up to  $5 \times 10^{12}$  ion/cm<sup>2</sup> while higher ion fluence  $\sim 5 \times 10^{13}$  ion/cm<sup>2</sup>, reduced in average grain size, after annihilation process. The effect of annihilation on charge conduction across ZnO/LGCMO p-n interface was studied by performed I-V characteristic using four probe method at room temperature. All the films exhibit non-linear I-V behavior and modifying conductivity under the annihilation effect due to the lattice strain which

gets suppressed (i.e. improved interface) as well as due to an average grain size that gets increased for ZnO/LGCMO films after annihilation process. Furthermore, I-V characteristics have been discussed in the context of improved lattice strain (i.e. interface), the average grain size and grain boundary density.

### Credit author statement

List of authors along with individual contribution as below:Alpa Zankat: Investigation, Data curation. Keval Gadani: Writing – original draft. Bhargav Rajyaguru: Visualization and Methodology. Khushal Sagapariya: Software. Vivek Pachchigar: Conceptualization. M. Ranjan: Resources. K. Asokan: Project administration. P.S. Solanki and N.A. Shah: Writing- Reviewing and Editing. D.D. Pandya: Supervision

### Declaration of competing interest

The authors declare that they have no known competing financial interests or personal relationships that could have appeared to influence the work reported in this paper.

### Acknowledgements

Authors AZ and DDP are thankful to Inter University Accelerator Centre, New Delhi for financial assistance in the form of research project [File No.: BTR 61304]. Authors are also thankful to Prof. Avinash Chandra Pandey, Inter University Accelerator Centre (IUAC), New Delhi for providing SHI irradiation facility. Authors are thankful to Dr. R.J. Choudhary and Dr. D.M. Phase, UGC-DAE Consortium for Scientific Research, Indore for providing pulsed laser deposition (PLD) facility.

### References

- [1] B.A. Hemdan, A.M. El Nahrawy, A.M. Mansour, A. Hammad, Green sol-gel synthesis of novel nanoporous copper alumino-silicate for the eradication of pathogenic microbes in drinking water and wastewater treatment, Environ. Sci. Pollut. Res. 26 (2019) 9508–9523.
- [2] M. Nasr, I.M. El Radaf, A.M. Mansour, Current transport and capacitance-voltage characteristics of an n-PbTe/p-GaP heterojunction prepared using the electron beams deposition technique, J. Phys. Chem. Solid. 115 (2018) 283–288.
- [3] A.M. Mansour, I.S. Yahia, I.M. El Radaf, Structural, electrical and photovoltaic properties of PbSb<sub>2</sub>S<sub>5</sub>/n-Si heterojunction synthesized by vacuum coating technique, Mater. Res. Express 5 (2018), 076406.
- [4] A.A.M. Farag, A.M. Mansour, A.H. Ammar, A. Abdel Rafea, Characterization of electrical and optical absorption of organic based methyl orange for photovoltaic application, Synth. Met. 161 (2011) 2135–2143.
- [5] E.M. El-Menyawy, A.M. Mansour, N.A. El-Ghamaz, S.A. El-Khadary, Electrical conduction mechanisms and thermal properties of 2-(2,3-dihydro-1,5-dimethyl-3-oxo-2-phenyl-1H-pyrazol-4-ylmino)-2-(4-nitropot) acetonitrile, Physica B 413 (2013) 31–35.
- [6] A.A.M. Farag, W.G. Osiris, A.H. Ammar, A.M. Mansour, Electrical and photo sensing performance of heterojunction device based on organic thin film structure, Synth. Met. 175 (2013) 81–87.
- [7] E.M. El-Menyawy, I.T. Zedan, A.M. Mansour, H.H. Nawar, Thermal stability, ac electrical conductivity and dielectric properties of N-(5-{{[abipyrrinyl-hydrazono]}-cyanomethyl}-[1,3,4] thiadiazol-2-yl)-benzamide, J. Alloys Compd. 611 (2014) 50–56.
- [8] A.A.M. Farag, F.S. Terra, A. Ashery, A.M. Mansour, Structural and electrical characterization of n-InAs/p-GaP heterojunctions prepared by vacuum flash evaporation and liquid phase epitaxy, Optoelectron. Adv. Mat. 11 (2017) 82–87.
- [9] A.A.M. Farag, F.S. Terra, A. Ashery, A.M. Mansour, Structural and electrical characteristics of n-InSb/p-GaAs heterojunction prepared by liquid phase epitaxy, J. Alloys Compd. 615 (2014) 604–609.
- [10] E.M. El-Menyawy, I.T. Zedan, A.M. Mansour, Electrical conductivity and dielectrical properties of bulk methlene green, J. Electron. Mater. 46 (2017) 4353–4358.
- [11] A.M. Mansour, F.M.A. El-Tawee, R.A.N. Abu El-Enein, E.M. El-Menyawy, Structural optical, electrical and photoelectrical properties of 2-Amino-4-5-(5-bromothiophen-2-yl)-5,6-dihydro-6-methyl-5-oxo4H-pyrano[3,2-c] quinoline-3-carbonitrile films, J. Electron. Mater. 46 (2017) 6957–6964.
- [12] I.M. El Radaf, Mahmoud Nasr, A.M. Mansour, Structural, electrical and photovoltaic properties of Co/Si heterojunction prepared by sprays pyrolysis, Mater. Res. Express 5 (2017), 015904.
- [13] A.A. Higazy, H. Afifi, A.H. Khafagy, M.A. El-Shahawy, A.M. Mansour, Ultrasonic studies on polystyrene/styrene butadiene rubber polymer blends filled with glass fiber and talc, Ultrasonics 44 (2006) e1439–e1445.
- [14] A.M. Mansour, Ali B. Abou Hammad, A.M. El Nahrawy, Sol-gel synthesis and physical characterization of novel MgCrO<sub>4</sub>-MgCu<sub>2</sub>O<sub>3</sub> layered films and MgCrO<sub>4</sub>-MgCu<sub>2</sub>O<sub>3</sub>/p-Si based photodiode, Nanostruct. Nano Obj. 25 (2021) 100646.
- [15] C. Zener, Interaction between the d-shells in the transition metals. II. Ferromagnetic compounds of manganese with perovskite structure, Phys. Rev. 82 (1950) 403–405.
- [16] W. Luo, M. Varela, J. Tao, S.J. Pennycook, S.T. Pantelides, Electronic and crystal-field effects in the fine structure of electron energy-loss spectra of manganites, Phys. Rev. B 79 (2009), 052405, 1–5.
- [17] A.J. Millis, P.B. Littlewood, B.I. Shraiman, Double exchange alone does not explain the resistivity of La<sub>1-x</sub>Sr<sub>x</sub>MnO<sub>3</sub>, Phys. Rev. Lett. 74 (1995) 5144–5147.
- [18] R.N. Parmar, J.H. Markna, P.S. Solanki, R.R. Doshi, P.S. Vachhani, D.G. Kuberkar, Grain size dependent transport and magnetoresistance behavior of chemical solution deposition grown nanostructured La<sub>0.7</sub>Sr<sub>0.3</sub>MnO<sub>3</sub> manganite films, J. Nanosci. Nanotechnol. 8 (2008) 4146–4151.
- [19] A. Krichene, W. Boujelben, S. Mukherjee, P.S. Solanki, N.A. Shah, Transport and magnetoresistance studies on polycrystalline, Acta Mater. 131 (2017) 491–498.
- [20] P.S. Solanki, R.R. Doshi, C.M. Thaker, S. Pandya, V. Ganesan, D.G. Kuberkar, Transport and magnetotransport studies on sol-gel grown nanostructured La<sub>0.7</sub>Pb<sub>0.3</sub>MnO<sub>3</sub> manganites, J. Nanosci. Nanotechnol. 9 (2009) 5681–5686.
- [21] S.B. Kansara, D. Dhruv, B. Kataria, C.M. Thaker, S. Rayaprol, C.L. Prajapat, M. R. Singh, P.S. Solanki, D.G. Kuberkar, N.A. Shah, Structural, transport and magnetic properties of monovalent doped La<sub>1-x</sub>Na<sub>x</sub>MnO<sub>3</sub> manganites, Ceram. Int. 41 (2015) 7162–7173.
- [22] A. Krichene, P.S. Solanki, S. Rayaprol, V. Ganesan, W. Boujelben, D.G. Kuberkar, B-site bismuth doping effect on structural, magnetic and magnetotransport properties of La<sub>0.5</sub>Ca<sub>0.5</sub>Mn<sub>1-x</sub>BixO<sub>3</sub>, Ceram. Int. 41 (2015) 2637–2647.
- [23] Sanjay Kansara, D.D. Pandya, Bhumiqa Nimavat, C.M. Thakar, P.S. Solanki, S. Raypro, M.R. Gonal, N.A. Shah, D.G. Kuberkar, Structure–transport correlations in mono-valent Na<sup>+</sup> doped La<sub>1-x</sub>Na<sub>x</sub>MnO<sub>3</sub> manganites, Adv. Mater. Res. 665 (2013) 1–7.
- [24] Zalak Joshi, D.D. Pandya, Davit Dhruv, Keval Gadani, Hetal Boricha, Sanjay Kansara, J.H. Markna, P.S. Solanki, N.A. Shah, Investigations on structural disorder-induced modifications in the transport behaviour of rare-earth manganites, Bull. Mater. Sci. 39 (2016) 1109–1117.
- [25] D.D. Pandya, Zalak Joshi, Davit Dhruv, Keval Gadani, Hetal Boricha, K.N. Rathod, Sanjay Kansara, J.H. Markna, P.S. Solanki, N.A. Shah, Structural and transport studies on mixed valent rare earth manganite ceramics, Trans. Indian Ceram. Soc. 76 (2017) 1–6.
- [26] Jalshikhaba S. Rathod, Uma Khachar, R.R. Doshi, P.S. Solanki, D.G. Kuberkar, Structural, transport and magnetotransport in nonmagnetic Al<sup>3+</sup> doped mixed valent La<sub>0.7</sub>Ca<sub>0.3</sub>Mn<sub>1-x</sub>Al<sub>x</sub>O<sub>3</sub> manganites, Int. J. Mod. Phys. B 26 (2012) 1–11, 1250136.
- [27] K.N. Rathod, Davit Dhruv, Keval Gadani, Hetal Boricha, Sapana Solanki, A. D. Joshi, D.D. Pandya, K. Asokan, P.S. Solanki, N.A. Shah, Comparison of charge transport studies of chemical solution and pulsed laser deposited manganite-based thin film devices, Appl. Phys. A 123 (2017) 1–8.
- [28] Davit Dhruv, Zalak Joshi, Sanjay Kansara, D.D. Pandya, J.H. Markna, K. Asokan, P. S. Solanki, D.G. Kuberkar, N.A. Shah, Temperature dependent I-V and C-V characteristics of chemically-grown Y<sub>0.95</sub>Ca<sub>0.05</sub>MnO<sub>3</sub>/Si thin films, Mater. Res. Express 3 (2016), 036402, 1–9.
- [29] Zalak Joshi, Davit Dhruv, K.N. Rathod, Hetal Boricha, Keval Gadani, D.D. Pandya, A.D. Joshi, P.S. Solanki, N.A. Shah, Low field magnetoelectric studies on sol-gel grown nanostructured YMnO<sub>3</sub> Manganites, Prog. Solid State Chem. 49 (2018) 23–26.
- [30] Z. Cheng, X. Wang, Room temperature magnetic-field manipulation of electrical polarization in multiferroic thin film Composite BiFeO<sub>3</sub>/La<sub>2/3</sub>Ca<sub>1/3</sub>MnO<sub>3</sub>, Phys. Rev. B 75 (2007) 1–4, 172406.
- [31] Alpa Zankat, Hetal Boricha, V.G. Shrimali, Keval Gadani, Khushal Sagapariya, Bhargav Rajyaguru, Manan Gal, D.D. Pandya, P.S. Solanki, N.A. Shah, Electrical properties of ZnO : ZnAlO nanoparticle matrix composites, J. Alloys Compd. 788 (2019) 623–631.
- [32] R.R. Doshi, P.S. Solanki, U. Khachar, D.G. Kuberkar, P.S.R. Krishna, A. Banerjee, P. Chadda, First order paramagnetic–ferromagnetic phase transition in Tb<sup>3+</sup> La<sub>0.5</sub>Ca<sub>0.5</sub>MnO<sub>3</sub> manganite, Physica B 406 (2011) 4031–4034.
- [33] R.R. Doshi, P.S. Solanki, P.S.R. Krishna, A. Das, D.G. Kuberkar, Magnetic phase coexistence in Tb<sup>3+</sup>- and Sr<sup>2+</sup>- doped La<sub>0.7</sub>Ca<sub>0.3</sub>MnO<sub>3</sub>: a temperature dependent neutron diffraction study, J. Magn. Magn. Mater. 321 (2009) 3285–3289.
- [34] A.B. Ravalia, M. V. Vagadia, P.G. Trivedi, P.S. Solanki, P.S. Vachhani, R. J. Choudhary, D.M. Phase, K. Asokan, N.A. Shah, D.G. Kuberkar, Modifications in device characteristics of La<sub>0.6</sub>Pr<sub>0.2</sub>Sr<sub>0.2</sub>MnO<sub>3</sub>/SrNb<sub>0.002</sub>Ti<sub>0.98</sub>O<sub>3</sub> manganite's by swift heavy ion irradiation, Indian J. Phys. 89 (2015) 137–142.
- [35] U. Khachar, P.S. Solanki, R.J. Choudhary, D.M. Phase, D.G. Kuberkar, Positive MR and large temperature–field sensitivity in manganite based heterostructures, J. Mater. Sci. Technol. 29 (2013) 989–994.
- [36] P.S. Solanki, Uma Khachar, Megha Vagadia, Ashish Ravalia, Savan Katba, D. G. Kuberkar, Electroresistance and field effect studies on manganite based heterostructure, J. Appl. Phys. 117 (2015) 1–6, 145306.
- [37] Uma Khachar, P.S. Solanki, S.B. Kansara, R.J. Choudhary, D.M. Phase, D. G. Kuberkar, N.A. Shah, Room temperature electroresistance across the interface in nanostructured ZnO/La<sub>0.7</sub>Sr<sub>0.3</sub>MnO<sub>3</sub>/SNTO heterostructures, IEEE TNANO 12 (2013) 915–918.
- [38] Davit Dhruv, Zalak Joshi, Keval Gadani, Sapana Solanki, J.H. Markna, A.D. Joshi, K. Asokan, P.S. Solanki, N.A. Shah, Transport properties of Y<sub>0.95</sub>Ca<sub>0.05</sub>MnO<sub>3</sub>/Si thin film junction, Physica B 518 (2017) 33–38.

- [39] J. Salafranca, M.J. Calderon, L. Brey, Magnetoresistance of an all–manganite spin valve: a thin antiferromagnetic insulator sandwiched between two ferromagnetic metallic electrodes, *Phys. Rev. B* 77 (2008), 014441, 1–5.
- [40] Z. Sefrioui, C. Visani, M.J. Calderon, K. March, C. Carretero, M. Walls, A. Rivera-Calzada, C. Leon, R.L. Anton, T.R. Charlton, F.A. Cuellar, E. Iborra, F. Ott, D. Imhoff, L. Brey, M. Bibes, J. Santamaría, A. Barthelemy, All–manganite tunnel junctions with interface–induced barrier magnetism, *Adv. Mater.* 22 (2010) 5029–5034.
- [41] Keval Gadani, Davit Dhruv, Zalak Joshi, Hetal Boricha, K.N. Rathod, M. J. Keshvani, N.A. Shah, P.S. Solanki, Transport properties and electroresistance of a manganite based heterostructure: role of the manganite–manganite interface, *Phys. Chem. Chem. Phys.* 18 (2016) 17740–17749.
- [42] Keval Gadani, M.J. Keshvani, Bhargav Rajyaguru, Davit Dhruv, B.R. Kataria, A. D. Joshi, K. Asokan, N.A. Shah, P.S. Solanki, Current–voltage characteristics and electroresistance in  $\text{LaMnO}_{3-\delta}/\text{La}_{0.7}\text{Ca}_{0.3}\text{MnO}_3/\text{LaAlO}_3$  thin film composites, *Phys. Chem. Chem. Phys.* 19 (2017) 29294–29304.
- [43] Khushal Sagapariya, Keval Gadani, K.N. Rathod, Zalak Joshi, Hetal Boricha, Davit Dhruv, M.J. Keshvani, Bhargav Rajyaguru, S.B. Kansara, A.D. Joshi, K. Asokan, P.S. Solanki, N.A. Shah, Charge transport in chemically grown manganite based heterostructure, *Mater. Chem. Phys.* 224 (2019) 229–237.
- [44] U.D. Khachar, P.S. Solanki, R.J. Choudhary, D.M. Phase, V. Ganeshan, D. G. Kuberkar, Room temperature positive magnetoresistance and field effect studies of manganite–based heterostructure, *Appl. Phys. A* 108 (2012) 733–738.
- [45] P.S. Solanki, R.R. Doshi, A. Ravalia, M.J. Keshvani, S. Pandya, V. Ganeshan, N. A. Shah, D.G. Kuberkar, Transport studies on  $\text{La}_{0.8-\delta}\text{Pr}_{0.2}\text{Sr}_x\text{MnO}_3$  manganite films, *Physica B* 465 (2015) 71–80.
- [46] T. Wu, S.B. Ogale, J.E. Garrison, B. Nagaraj, A. Biswas, Z. Chen, R.L. Greene, R. Ramesh, T. Venkatesan, Electroresistance and electronic phase separation in mixed–valent manganites, *Phys. Rev. Lett.* 86 (2001) 5998–6001.
- [47] A.K. Pramanik, A. Banerjee, Phase separation and the effect of quenched disorder in  $\text{Pr}_{0.5}\text{Sr}_{0.5}\text{MnO}_3$ , *J. Phys. Condens. Matter* 20 (2008) 1–10, 275207.
- [48] P.K. Siwach, U.K. Goutam, P. Srivastava, H.K. Singh, R.S. Tiwari, O.N. Srivastava, Colossal magnetoresistance study in nanophasic  $\text{La}_{0.7}\text{Ca}_{0.3}\text{MnO}_3$  manganite, *J. Phys. D Appl. Phys.* 39 (2006) 14–20.
- [49] D.G. Kuberkar, R.R. Doshi, P.S. Solanki, U. Khachar, M. Vagadia, A. Ravalia, V. Ganeshan, Grain morphology and size disorder effect on the transport and magnetotransport in sol–gel grown nanostructured manganites, *Appl. Surf. Sci.* 258 (2012) 9041–9046.
- [50] X.G. Chen, J.B. Fu, S.Q. Liu, Y.B. Yang, C.S. Wang, H.L. Du, G.C. Xiong, G.J. Lian, J. B. Yang, Trap-assisted tunneling resistance switching effect in  $\text{CeO}_2/\text{La}_{0.7}(\text{Sr}_{0.1}\text{Ca}_{0.9})_{0.3}\text{MnO}_3$  heterostructure, *Appl. Phys. Lett.* 101 (2012) 1–4, 153509.
- [51] W. Ramadan, S.B. Ogale, S. Dhar, S.X. Zhang, D.C. Kundaliya, I. Satoh, T. Venkatesan, Substrate-induced strain effects on the transport properties of pulsed laser-deposited Nb-doped  $\text{SrTiO}_3$  films, *Appl. Phys. Lett.* 88 (2006) 1–3, 142903.
- [52] S. Jacob, T. Roch, F.S. Razavia, G.M. Gross, H.U. Habermeier, The thickness dependence of the effect of pressures on magnetic and electronic properties of thin films of  $\text{La}_{2/3}\text{Ca}_{1/3}\text{MnO}_3$ , *J. Appl. Phys.* 91 (2002) 2232–2235.
- [53] Ashish Ravalia, Megha Vagadia, Priyanka Trivedi, M.J. Keshvani, Uma Khachar, B. T. Savalia, P.S. Solanki, K. Asokan, D.G. Kuberkar, Swift heavy ion irradiation studies on the transport in  $\text{La}_{0.8-x}\text{Pr}_{0.2}\text{Sr}_x\text{MnO}_3$ , *Adv. Mater. Res.* 665 (2013) 63–69.
- [54] Malay Udeshi, Brinda Vyasa, Priyanka Trivedi, Savan Katba, Ashish Ravalia, P. S. Solanki, N.A. Shah, K. Asokan, S. Ojha, D.G. Kuberkar, Investigation on the dielectric response of  $\text{NdMnO}_3/\text{LSAT}$  thin films: effect of 200 MeV  $\text{Ag}^{+15}$  ion irradiation, *NIMB* 365 (2015) 560–563.
- [55] Keval Gadani, K.N. Rathod, Davit Dhruv, Hetal Boricha, Khushal Sagapariya, A. D. Joshi, D.D. Pandya, K. Asokan, P.S. Solanki, N.A. Shah, Defect dynamics in the resistive switching characteristics of  $\text{Y}_{0.95}\text{Sr}_{0.05}\text{MnO}_3$  films induced by electronic excitations, *J. Alloys Compd.* 788 (2019) 819–830.
- [56] Bharvi Hirpara, Keval Gadani, Khushal Sagapariya, Hardik Gohil, Drashti Sanghvi, A.D. Joshi, K. Asokan, P.S. Solanki, N.A. Shah, Resistive switching effect and charge conduction mechanisms in  $\text{Y}_{0.95}\text{Sr}_{0.05}\text{MnO}_3$  manganites : dynamic role of defects, *Thin Solid Films* 685 (2019) 151–160.
- [57] K.N. Rathod, Keval Gadani, Davit Dhruv, Hetal Boricha, Alpa Zankat, A.D. Joshi, J. P. Singh, K. K H Chae, P.S. Solanki Asokan, N.A. Shah, Investigations on the electronic excitations through spectroscopic measures for resistive switching character of manganite thin films, *Phys. Status Solidi B* (2019) 1–9, 1900264.
- [58] Neeti Tripathi, Shyama Rath, Effect of thermal annealing and swift heavy ion irradiation on the optical properties of indium oxide thin films, *ECS J Solid State Sci. Technol.* 3 (2014) 21–25.
- [59] Z.H. Wu, Q. Wang, W.D. Yu, D.S. Shang, X.M. Li, L.D. Chen, Resistance and magnetization of  $\text{La}_{0.7}\text{Ca}_{0.3}\text{MnO}_3$  bulk at different resistance states induced by electric pulses, *J. Phys. D Appl. Phys.* 41 (2008) 1–4, 025401.
- [60] P.S. Vachani, P.S. Solanki, J.H. Markna, R.N. Parmar, J.A. Bhalodia, D.G. Kuberkar, Strain induced non–linear conduction in epitaxial  $\text{La}_{0.7}\text{A}_{0.3}\text{MnO}_3$  manganite thin films, *Indian J. Eng. Mater. Sci.* 17 (2007) 163–166.
- [61] P. Dey, T.K. Nath, Effect of grain size modulation on the magneto– and electronic–transport properties of  $\text{La}_{0.7}\text{Ca}_{0.3}\text{MnO}_3$  nanoparticles : the role of spin–polarized tunneling at the enhanced grain surface, *Phys. Rev. B* 73 (2006) 1–14, 214425.
- [62] J.S. Rathod, M.J. Keshvani, P.S. Solanki, D.D. Pandya, Bharat Kataria, N.A. Shah, D.G. Kuberkar, Studies on charge transport in Al-doped  $\text{La}_{0.7}\text{Ca}_{0.3}\text{Mn}_{1-x}\text{Al}_x\text{MnO}_3$  manganites, *Physica B* 478 (2015) 1–5.
- [63] Bharavi Hirpara, Keval Gadani, Khushal Sagapariya, Hardik Gohil, Drashti Sanghvi, A.D. Joshi, K. Asokan, P.S. Solanki, N.A. Shah, Resistive switching effect and charge conduction mechanisms in  $\text{Y}_{0.95}\text{Sr}_{0.05}\text{MnO}_3$  manganites: dynamic role of defects, *Thin Solid Films* 685 (2019) 151–160.
- [64] S.M. Sze, Physics of Semiconductor Devices, second ed., Wiley, New York, 1981.
- [65] D.J. Wang, J.R. Sun, Y.W. Xie, W.M. Lu, S. Liang, T.Y. Zhao, B.G. Shen, Magnetic field effects on the manganite junction with different electronic processes, *Appl. Phys. Lett.* 91 (2007), 062503, 1–3.
- [66] V.R. Rayapati, D. Burger, N. Du, R. Patra, I. Skorupa, D. Blaschke, H. Stocker, P. Matthes, S.E. Schulz, H. Schmidt, Electroforming-free resistive in yttrium manganite thin films by cationic substitution, *J. Appl. Phys.* 126 (2019), 074102, 1–10.
- [67] T. Polek, M. Semenko, T. Endo, Y. Nakamura, G.S. Lotey, A. Tsvetlykin, ESR study of  $(\text{La},\text{Ba})\text{MnO}_3/\text{ZnO}$  nanostructure for resistive switching device, *Nano Res. Lett.* 12 (2017) 180, 1–7.